Structure and optical properties of layered perovskite $(MA)_2PbI_{2-x}Br_x(SCN)_2$ ($0 \le x < 1.6$)

Takafumi Yamamoto[1,2,*], Iain W. H. Oswald[3], Christopher Savory[4], Takuya Ohmi,[1] Alexandra A. Koegel[3], David O. Scanlon[4],Hiroshi Kageyama[2,5] and James R. Neilson[3,*]

[1] Laboratory for Materials and Structures, Tokyo Institute of Technology, Yokohama, 226-8503, Japan

[2] Department of Energy and Hydrocarbon Chemistry, Graduate school of Engineering, Kyoto University, Kyoto 615-8510, Japan

[3] Department of Chemistry, Colorado State University, Fort Collins, CO, 80523-1872, United States

[4] Department of Chemistry, University College London, 20 Gordon Street, London, WC1H 0AJ, United Kingdom

[5] CREST, Japan Science and Technology Agency (JST), Kawaguchi, Saitama 332-0012, Japan

ABSTRACT: The layered perovskite $(MA)_2PbI_2(SCN)_2$ ($MA = CH_3NH_3^+$) is a member of an emerging series of compounds derived from the hybrid organic-inorganic perovskites. Here, we successfully synthesized $(MA)_2PbI_{2-x}Br_x(SCN)_2$ ($0 \le x < 1.6$) by using a solid state reaction. Despite smaller bromide substitution for iodine, 1% linear expansion along the *a* axis was observed at $x \sim 0.4$ due to a change of the orientation of the SCN^- anions. Diffuse reflectance spectra reveal that the optical band gap increases by the bromide substitution, which is supported by the DFT calculations. Curiously, bromine-rich compounds where $x \ge 0.8$ are light sensitive leading to partial decomposition after ~24 h. This study demonstrates that the layered perovskite $(MA)_2PbI_2(SCN)_2$ tolerates a wide range of bromide substitution toward tuning the band gap energy.

1. Introduction

Layered hybrid organic-inorganic perovskites have recently attracted attention for their promising properties for photovoltaic, radiation detection, lasing, and light emission applications.[1-12] The Ruddlesden-Popper-type layered perovskite with a general formula $A'_2A_{n-1}B_nX_{3n+1}$ consists of corner-shared two-dimensional (2D) perovskite layers ($A_{n-1}B_nX_{3n+1}$) and interlayer cation A', where A' and A is organic or inorganic cation; B is a main-group cation; X is halide; *n* is an integer. Since the interlayer space is flexible, the A' cation can accommodate a variety of organic cations, including bulky cations such as decylammonium or phenylethylammonium.[5,13] This is different from the three-dimensional (3D) ABX_3 perovskite where the A-site space is determined by the size of B and X ions. Such a tolerance of the chemical composition in the layered perovskite is advantageous for tuning their properties.[2,3,12]

Furthermore, this structural framework can also accommodate bulky anions. While cyanide, formate, and hypophosphite linkers can adopt three-dimensional perovskite-like frameworks,[14] the mixing of anions can drive dimensional reduction. $(MA)_2PbI_2(SCN)_2$ ($MA = CH_3NH_3^+$) adopts a $n = 1$ layered Ruddlesden-Popper perovskite derived structure with two different anions I^- and SCN^- (Figure 1).[15,16] The anions are fully ordered where bulky SCN^- lies in the apical site. S is bonded to Pb^{2+} and the SCN chain is directed to the interlayer space where the angle of ∠Pb-S-C is 103.5°.[16] The optical band gap was originally reported as 1.57 eV,[15] but a subsequent study on a thin film[17] and a single crystal[16,18] samples suggested that the intrinsic band gap is ~2.1 eV. MA-site substitution for Cs drastically changes the band structure, leading changing photo-response.[19] In addition, mixed-halide $Cs_2PbI_{2-x}Br_x(SCN)_2$ allows to tune the band gap from 2.1 eV to 2.7 eV.[19] Further investigation into this system is of interest to control the optical properties, although the halide-site substitution of $(MA)_2PbI_2(SCN)_2$ was not reported so far.

Herein, we report bromide substitution for $(MA)_2PbI_2(SCN)_2$. We found that, using solid state reactions, approximately 80% bromide substitution for iodine is possible. Unexpectedly, a 1% linear expansion along the *a* axis was observed at $x \sim 0.4$ despite smaller bromide substitution. Single crystal X-ray diffraction (XRD) measurement revealed that the expansion is derived from a change in the orientation of the SCN^- anions. Diffuse reflectance spectra reveal that the optical band gap increases by the bromide substitution.

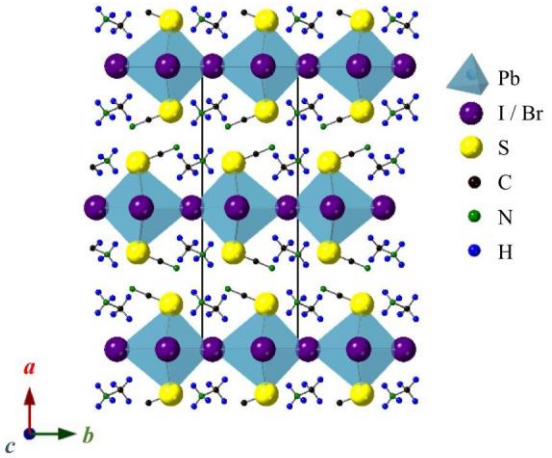

Figure 1. Structure of $(MA)_2PbI_{2-x}Br_x(SCN)_2$.

2. Experimental Procedure

Methylammonium iodide (MAI) and methylammonium bromide (MABr) were synthesized by dissolving 1 g of methylammonium chloride (99 %, BTC) powder in 4 ml of 57 %w/w hydroiodic acid (for MAI) or 4 ml of 48 %w/w hydrobromic acid (for MABr). After addition of acid the solution was left stirring for 5 minutes at 50 °C with adding 3ml of ethanol. Then, cooling in the iced bath with adding 30 ml of diethyl ether. Plate-like white precipitates were washed with diethyl ether and dried at 60 °C for overnight. Lead thiocyanate $Pb(SCN)_2$ was synthesized by dissolving 0.9027 g of KSCN (98.5%, Alfa Aesar; 9.279 mmol) and 1.5366 g of $Pb(NO_3)_2$ (99%, Alfa Aesar; 4.639 mmol) in 10 ml of distilled water. White precipitates of $Pb(SCN)_2$ were filtered and dried at 60 °C for overnight. $Pb(SCN)_2$ was stored away from light.

Powder samples of $(MA)_2PbI_{2-x}Br_x(SCN)_2$ (x = 0, 0.4, 0.8, 1.2, 1.6, 2.0) were prepared by using solid state synthesis. Stoichiometric amount of MAI, MABr, and $Pb(SCN)_2$ were mixed and pelletized. The pellets of x = 0, 0.4, 0.8, 1.2 were heated at 50 °C for 24 hours with an intermediate grinding (12+12 hours heating of the pellets). The pellets of x = 1.6, 2.0 were heated at 30 °C for 24 hours with an intermediate grinding since they melted at 50 °C. Single crystal of $(MA)_2Pb(I_{2-x}Br_x)(SCN)_2$ (x = 0.4) was prepared by solid state reaction of stoichiometric amount of precursors at 100 °C.

Powder X-Ray diffraction (PXRD) data were collected on a Bruker D8 Discover DaVinci Powder X-ray diffractometer using Cu *K*α radiation and a Lynxeye XE-T position-sensitive detector. Samples were prepared on a "zero-diffraction" Si wafer by sprinkling the microcrystalline powder directly onto the substrate. The lattice parameters were calculated by Le Bail fitting with TOPAS v5 software. High-resolution synchrotron XRD experiments for x = 0, 0.4, 0.8, and 1.2 were performed at 300 K using the large Debye-Scherrer cameras with a semiconductor detector installed at the beamline BL02B2 (JASRI, SPring-8). Incident beams from a bending magnet were monochromatized to λ = 0.421018(1) Å and 0.779570(1) Å for x = 0, 0.4 and x = 0.8, 1.2, respectively. Finely ground powder samples were sieved through a 32-μm mesh sieve and were packed into Pyrex capillaries with an inner diameter of 0.2 mm, which were then sealed. The sealed capillary was rotated during measurements to improve randomization of the individual crystallite orientations. The Rietveld refinements were performed by Rietan-FP software.[20]

Single crystal XRD data of x = 0.4 was collected at room temperature using a Bruker D8 Quest ECO diffractometer equipped with a microfocus Mo Kα radiation source and Photon 50 CMOS half-plate detector. Single crystals were mounted onto a glass fiber with 5-minute epoxy. Bruker SAINT was used for integration and scaling of collected data and SADABS was used for absorption correction.[21] Starting models for the compounds were generated using the intrinsic phasing method in SHELXT.[22] SHELXL2014 was used for least-squares refinement.[23] The PLATON suite was used to determine higher symmetry and for structural validation.[24] Structural details of the refinement, crystallographic parameters, and atomic positions can be found in Tables S1 and S2 in Supporting Information.

UV-visible diffuse reflectance spectra were collected on powdered samples of each compound using an Agilent (Cary) 500 Scan UV-Vis-NIR spectrophotometer with a Praying Mantis mirror setup from λ = 350 to 1000 nm. FT-IR spectra of the powder samples were obtained by using Nicolet iS-50 FT-IR spectrometer.

DFT calculations for $(MA)_2PbI_{2-x}Br_x(SCN)_2$ (x = 0.5, 1.0, 1.5) were performed using the Vienna Ab initio Simulation Package (VASP),[25-28] with interactions between the core and valence electrons described using the Projector Augmented Wave (PAW) method.[29] Electronic properties were calculated using the Heyd–Scuseria–Ernzerhof (HSE06) hybrid DFT functional[30] with the addition of spin orbit effects, which is known to accurately predict the properties of hybrid halide perovskite systems.[31] Both *k*-point sampling and the plane wave basis set were checked for convergence, with a cutoff of 520 eV and k-point grid of Γ-centered 1 × 4 × 4 for the 50 atom unit cell. All structures were geometrically optimized and considered to be converged when the forces on all the atoms totaled less than 10 meV Å^{-1}. All theoretical electronic structure and optical figures in this work were plotted with the aid of the sumo package.[32]

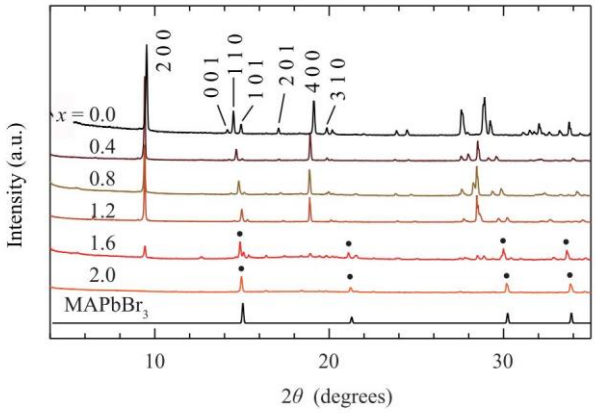

Figure 2. XRD patterns of $(MA)_2PbI_{2-x}Br_x(SCN)_2$ (x = 0, 0.4, 0.8, 1.2, 1.6, 2.0). • indicates peaks from perovskite $MAPb(I,Br)_3$ phases. Simulation pattern of $MAPbBr_3$ is shown for comparison.[33]

3. Results and Discussions

The laboratory XRD pattern of the samples for nominal values of x = 0, 0.4, 0.8, 1.2, 1.6, and 2.0 are shown in Figure 2. The patterns for x = 0.4, 0.8, and 1.2 are similar with $(MA)_2PbI_2(SCN)_2$ (x = 0)[15,16] suggesting formation of $(MA)_2PbI_{2-x}Br_x(SCN)_2$ phase. These patterns can be indexed using Orthorhombic unit cell (SG; $Pmn2_1$, a ~ 18.6 Å b ~ 6.4 Å, c ~ 6.2 Å),[16] which is the same cell as x = 0, with tiny unknown impurity peaks. The pattern for x = 2.0 can be assigned as the peaks from perovskite $MAPbBr_3$ and $Pb(SCN)_2$ with unknown impurities (Figure S1 in Supporting information). The sample for x = 1.6 includes $(MA)_2PbI_{2-x}Br_x(SCN)_2$ phase with perovskite $MAPb(I,Br)_3$, suggesting the solubility limit of x ~ 1.6. The sample for x = 0.8, and 1.2 are light sensitive: It partially decomposes under light irradiation to reveal Pb^0 (Figure S2). This trend in stability is opposite to what is observed in the $MAPbI_3$ vs $MAPbBr_3$, in that the $MAPbI_3$ is more light sensitive;[34] however, mixed anion $MAPbI_{3-x}Br_x$ phases exhibit phase separation under light exposure due to the destabilizing chemical pressure.[35,36]

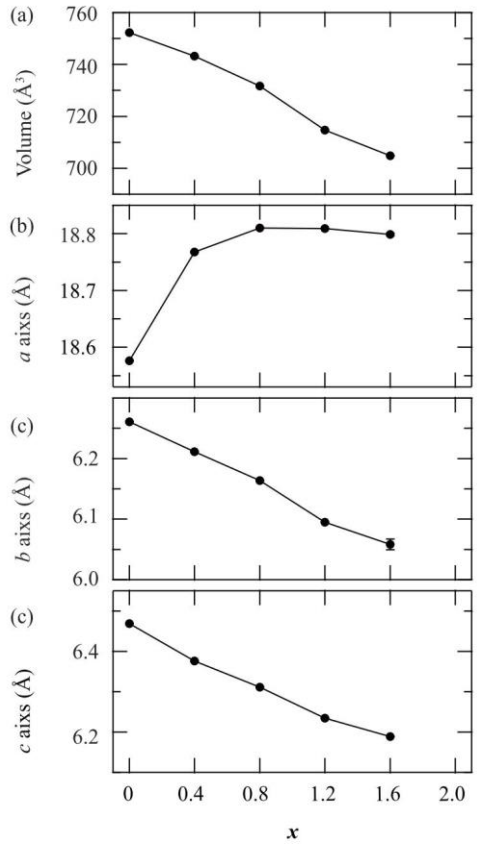

Figure 3. Lattice parameters and volume of $(MA)_2PbI_{2-x}Br_x(SCN)_2$ as a function of x.

As shown in Figure 2, some peaks, such as 001, 110, and 101, shift to higher angle with increase of x, in consistency with small Br-substitution. However, the 200 and 400 peaks shift to lower angle from $x = 0$ ($2\theta = 9.54°$) to 0.4 ($2\theta = 9.43°$) and closely maintain the same angle in $x \geq 0.4$. This suggests the a axis increases by Br-substitution at $x \leq \sim 0.4$. As expected, the peak shifts in the b and c axes decrease while the a axis increases by Br-substitution (Figure 3). Namely, linear expansion occurs by applying chemical pressure. Note that the volume decreases linearly with increasing x, which is consistent with Vegard's law. The a axis expands by 1.0% ($x = 0.4$) Br substitution, while the b and c axes decrease by 0.85% and 1.5%, respectively. The a axis expansion is nearly saturated above $x \sim 0.8$.

The single crystal XRD measurement for $x = 0.4$ revealed the crystal structure (Tables S1 and S2), with a refined composition of $(MA)_2PbI_{1.59(2)}Br_{0.41(2)}(SCN)_2$. There are two halide sites, where I1/Br1 and I2/Br2 bond to Pb along the b and c axes, respectively. The Pb-I1/Br1 distances (3.124(1) Å and 3.086(1) Å) are shorter than the Pb-I2/Br2 distances (3.201(6) Å and 3.195(6)), in consistency with the lattice parameters. In $x = 0$, the bond lengths are more asymmetrical, where $d_{Pb\text{-}I1}$ = 3.1453(7) Å and 3.1462(7) Å and $d_{Pb\text{-}I2}$ = are 3.293(1) Å and 3.183(1) Å.[16] The occupancy of Br^- in I2/Br2 ($g_{Br2} = 0.222(13)$) is slightly larger than the other site ($g_{Br1} = 0.191(14)$), which is opposite to the bond length. This is possibly related with interaction between I^-/Br^- and SCN^-, where the SCN^- ion is close to the I1/Br1 site. The bond distances in the SCN^- anions are quite similar between $x = 0$ and 0.4, where C-N distances are 1.17(1) Å ($x = 0$) and 1.19(3) Å ($x = 0.4$) and S-C distances are 1.60(1) Å ($x = 0$) and 1.59(2) Å ($x = 0.4$).

The IR bands around ~ 2100 cm^{-1} correspond to CN stretches (Figure S3).[37] 2098 cm^{-1} at the peak for $x = 0$ is consistent with the previous studies.[15,38] The double band feature (peaks with 2098 cm^{-1} and 2115 cm^{-1}) can possibly be explained by the vibrational coupling or vibrational excitation transfer between two adjacent SCN^- anions.[38] The peak position shifts to higher wavenumber with increase of x, suggesting stronger C-N bond. Simultaneously, the band becomes broader with increasing x, indicating the CN stretches becomes limited by a decrease of the volume of the interlayer space.

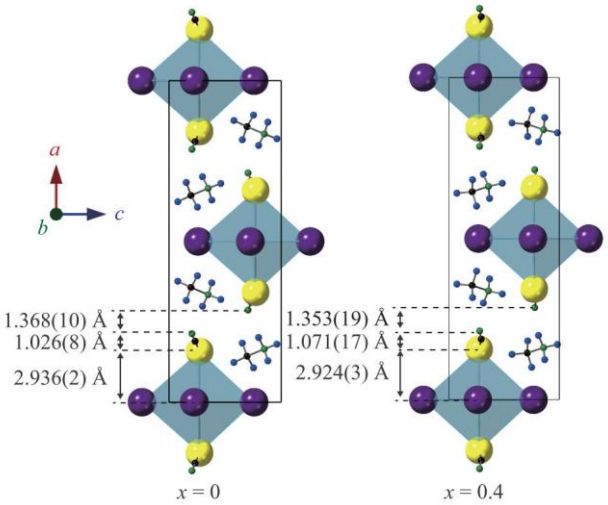

Figure 4. Structure comparison between $x = 0$ and 0.4 of $(MA)_2PbI_{2-x}Br_x(SCN)_2$. The heights along the a axis are shown.

The linear expansion along the a axis can be rationalized by a change of the orientation of SCN^- anion by Br-substitution. Figure 4 shows the heights of the atoms along the a axis. The height of SCN^- anion along the a axis clearly increases with Br-substitution. This increase is mainly derived from orientation of SCN^- anion along the a axis since bond distances in the SCN^- anions are quite the same. In fact, the angle of (pseudo-linear) SCN^- anion from the bc plane increases from 21.8(2)° for $x = 0$ to 22.8(3)° for $x = 0.4$. Note that the height of Pb-S slightly deceases by Br-substitution due to decrease of Pb-S bond distance from 2.964(3) Å for $x = 0$ to 2.960(4) Å for $x = 0.4$ with increase of the distortion of PbX_4S_2 octahedra (X = I or Br). However, the increase by SCN^- anion is superior to slight decrease of the Pb-S height. Thus, the molecular anion, SCN^-, plays important a role for the linear expansion along the a axis. In some molecular complex materials, such as MIL-53 and $Ag_3[Co(CN)]_6$,[39,40] negative linear compressibility was reported by the so called 'wine-rack' mechanism; relative orientations of the molecular framework play a key role.[41] Although a negative linear compressibility was not reported in $(MA)_2PbI_2(SCN)_2$,[16] the material having molecular ions, like the present compound, may be advantageous for seeking a compound with negative linear compressibility.

We also performed synchrotron XRD measurements for x = 0, 0.4, 0.8, and 1.2 at 300K (Figure S4). Rietveld refinement was carried out assuming the $(MA)_2PbI_2(SCN)_2$ structure (SG;

*Pmn*2$_1$) obtained by single crystal diffraction.[15] The refinements for x = 0 and 0.4 converged reasonably, with the goodness-of-fit indicator S = 2.82 and 3.78, respectively (Figure S5 and Table S3 and S4). However, the refinements for x = 0.8 and 1.2 did not converge (S > 8), possibly due to highly disordered structures or poor crystallinity. It should be noted that structural refinement of the single crystal for x = 0.8 was also unsuccessful. Further investigation is needed for understanding the structure of highly Br-substituted samples. The interesting difference between the single crystal and powder samples for x = 0.4 is anion distribution. The occupancy of Br^- in I1/Br1 (g_{Br} = 0.26(2)) for the powder sample is larger than the other site (g_{Br} = 0.14(2)), which is opposite to the trend obtained by single crystal sample. Since the reaction temperatures are different (50 °C and 100 °C for powder and single crystal, respectively), the anion distribution may be able to control the reaction procedures, as anion order can be engineered in complex layered perovskite derivatives.[42] Note that the slightly different lattice parameters between the powder (a = 18.7675(5) Å, b =6.2112(3) Å, c = 6.3758(2) Å) and single crystal (a = 18.686(5) Å, b = 6.2090(16) Å, c = 6.875(17) Å) support existence of structural difference between them. In addition, we obtained a powder sample with the similar lattice parameters to the single crystal by heating the powder at 100 °C (Figure S6).

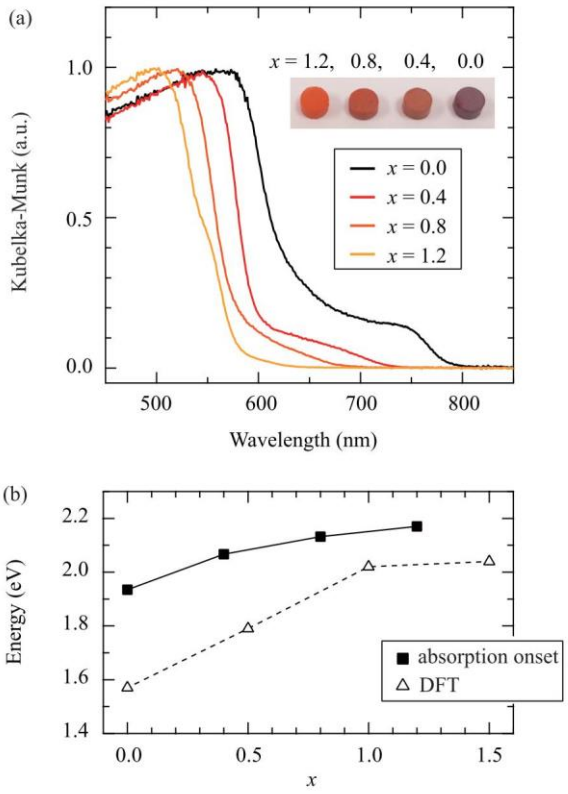

Figure 5. Diffuse reflectance spectra (a) and optical gap energy (b) of $(MA)_2PbI_{2-x}Br_x(SCN)_2$. Inset in (a) show the pellets of the powder samples. The optical gaps for onset region in (b) are determined by the intersection of linear fitting curves of the baseline and onset regions of the data. Indirect gap obtained DFT calculations are also shown in (b), where the value for x = 0 is from ref 43. .

UV−visible diffuse reflectance spectra performed on powdered samples show a blue shift with increasing bromide content (Figure 5a), suggesting an increase of the band gap. The absorption edges are observed at approximately 790, 730, 680, and 620 nm for x = 0, 0.4, 0.8, and 1.2, respectively. However, according to the previous studies, [16-18,44] this low energy absorption may be attributed to trace impurities (e.g., $MAPbI_3$, though undetectable by synchrotron XRD) or defect states. The intrinsic band gap of $(MA)_2PbI_2(SCN)_2$ was reported as ~2.1 eV,[16-18,44] which roughly corresponds to onset region of the sharp absorption at around 600 nm (x = 0). Figure 5b shows x dependence of the onset region, which is determined by the intersection of linear fitting curves of the baseline and onset regions of the spectra. The onset region, which roughly corresponds to optical gap, monotonically increase with x. This tendency was also reported in $Cs_2PbI_{2-x}Br_x(SCN)_2$.[19]

We carried out DFT calculations for x = 0.5, 1.0, and 1.5 (Figures 6 and S7). We considered all possible structures of the symmetrically independent I/Br configurations within the unit cell and found 2, 4, and 2 non-equivalent configurations of for the x = 0.5, 1.0, and 1.5 compositions, respectively (Figure S8). No particular energetic preference for anion ordering was seen for all the possible configurations, with the total energies of all ordered structures for each composition within 25 meV of each other after relaxation, which is consistent to the experimental result of the disordering of anion site in x = 0.4. Thus, we took the average over all the electronic structures for each composition, giving HSE06+SOC indirect gaps of 1.79 eV (direct gap of 1.80 eV), 2.02 eV (2.06 eV), and 2.04 eV (2.10 eV), for x = 0.5, 1.0, and 1.5, respectively. These values are slightly underestimated since this study does not use an increased percentage of Hartree-Fock exchange in the HSE06 functional, which was used by Xiao et al. to obtain a 2.1 eV theoretical band gap for $(MA)_2PbI_2(SCN)_2$.[17] Increased exchange was not used here as, while the rigid shift in band gap with higher exact exchange would lead to a closer agreement with experimental optical gaps for the pure iodide phase, it would lead to significant overestimation at increased bromide concentrations; standard HSE06 has previously showed a consistent description of the band edge effects in other perovskite-derived bromide/iodide mixed systems,[42,45] and remains consistent with DFT calculations of related pseudohalide systems.[46] However the tendency towards higher gaps with higher Br substitution is consistent with the experimental optical gaps (Figure 5b), and may primarily result from the reduction in the splitting of both the valence and conduction bands around the E_0 and A_0 points in the Brillouin zone as the contribution from Br increasingly dominates, widening the gap.

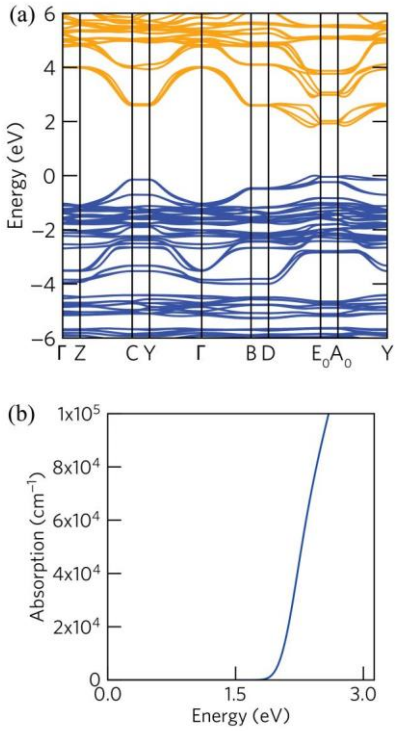

Figure 6. (a) Calculated HSE06+SOC band structure along the high symmetry directions and (b) absorption for the lowest energy polymorph of $(MA)_2PbI_{1.5}Br_{0.5}(SCN)_2$ (x = 0.5). The high symmetry points in this figure use the definitions of Bradley and Cracknell.[47]

4. Conclusion

Using a solid state reaction, $(MA)_2PbI_{2-x}Br_x(SCN)_2$ ($0 \le x < 1.6$) was successfully synthesized. Structural characterization revealed a linear expansion of along the *a* axis at $x \sim 0.4$, which is derived from change of orientation of the molecular anion by shrinkage of the *bc* plane. Diffuse reflectance spectra showed that the optical band gap increases by the bromide substitution, which is supported by the DFT calculations. Compounds with significant bromine content ($x \ge 0.8$) are light sensitive and partially decompose after ~24 h of room light exposure. This study demonstrates that the layered perovskite $(MA)_2PbI_2(SCN)_2$ tolerates wide range of bromide substitution toward tuning the band gap energy.

ASSOCIATED CONTENT

Supporting Information

Supporting graphics and tables. This material is available free of charge via the Internet at http://pubs.acs.org.

Crystallographic data of $(MA)_2PbI_{1.6}Br_{0.4}(SCN)_2$ (CCDC 2023483)

AUTHOR INFORMATION

Corresponding Author

* to whom correspondence should be addressed:
yama@msl.titech.ac.jp
James.Neilson@colostate.edu

Notes

The authors declare no competing financial interests.

ACKNOWLEDGMENT

This work was supported by JSPS KAKENHI Grant Numbers JP16H06438, JP16H06439, JP16H06440, 16K21724. This work was also supported by CREST (JPMJCR1421). Work at Colorado State University was supported by the U.S. Department of Energy, Office of Science, Basic Energy Sciences, under Award SC0016083. J.R.N. and I. W. H. O. also acknowledge support from Research Corporation for Science Advancement through a Cottrell Scholar Award and the A.P. Sloan Foundation for assistance provided from a Sloan Research Fellowship. The use of the UCL Legion, Myriad and Grace High Performance Computing Facilities (Legion@UCL, Myriad@UCL and Grace@UCL) are acknowledged in the production of this work. Computational work was also performed on the ARCHER UK National Supercomputing Service, via our membership of the UK's HEC Materials Chemistry Consortium, funded by EPSRC (EP/L000202/1 and EP/R029431/1). The synchrotron radiation experiments were performed at the BL02B2 of SPring-8 with the approval of the Japan Synchrotron Radiation Research Institute (JASRI) (Proposal No. 2019A1104).

References

1. Calabrese, J.; Jones, N.; Harlow, R.; Herron, N.; Thorn, D.; Wang, Y. Preparation and characterization of layered lead halide compounds. *J. Am. Chem. Soc.* **1991**, *113*, 2328-2330.

2. Mitzi, D. B.; Feild, C.; Harrison, W.; Guloy, A. Conducting tin halides with a layered organic-based perovskite structure. *Nature* **1994**, *369*, 467-469.

3. Mitzi, D. B.; Wang, S.; Feild, C. A.; Chess, C. A.; Guloy, A. M. Conducting Layered Organic-inorganic Halides Containing −Oriented Perovskite Sheets. *Science* **1995**, *267*, 1473-1476.

4. Wang, S.; Mitzi, D. B.; Feild, C. A.; Guloy, A. Synthesis and characterization of $[NH_2C(I)=NH_2]_3MI_5$ (M= Sn, Pb): stereochemical activity in divalent tin and lead halides containing single perovskite sheets. *J. Am. Chem. Soc.* **1995**, *117*, 5297-5302.

5. Kagan, C. R.; Mitzi, D. B.; Dimitrakopoulos, C. D. Organic-inorganic hybrid materials as semiconducting channels in thin-film field-effect transistors. *Science* **1999**, *286*, 945-947.

6. Dohner, E. R.; Hoke, E. T.; Karunadasa, H. I. Self-assembly of broadband white-light emitters. *J. Am. Chem. Soc.* **2014**, *136*, 1718-1721.

7. Dohner, E. R.; Jaffe, A.; Bradshaw, L. R.; Karunadasa, H. I. Intrinsic white-light emission from layered hybrid perovskites. *J. Am. Chem. Soc.* **2014**, *136*, 13154-13157.

8. Smith, I. C.; Hoke, E. T.; Solis-Ibarra, D.; McGehee, M. D.; Karunadasa, H. I. A layered hybrid perovskite solar-cell absorber with enhanced moisture stability. *Angew. Chem. Int. Ed.* **2014***, 126*, 11414-11417.

9. Dou, L.; Wong, A. B.; Yu, Y.; Lai, M.; Kornienko, N.; Eaton, S. W.; Fu, A.; Bischak, C. G.; Ma, J.; Ding, T.; Ginsberg, N. S.; Wang, L. W.; Alivisatos, A. P.; Yang, P. Atomically thin two-dimensional organic-inorganic hybrid perovskites. *Science* **2015***, 349*, 1518-1521.

10. Tsai, H.; Nie, W.; Blancon, J.; Stoumpos, C. C.; Asadpour, R.; Harutyunyan, B.; Neukirch, A. J.; Verduzco, R.; Crochet, J. J.; Tretiak, S.; Pedesseau, L.; Even, J.; Alam, M. A.; Gupta, G.; Lou, J.; Ajayan, P. M.; Bedzyk, M. J.; Kanatzidis, M. G.; Mohite, A. D. High-efficiency two-dimensional Ruddlesden–Popper perovskite solar cells. *Nature* **2016***, 536*, 312-316.

11. Blancon, J. C.; Tsai, H.; Nie, W.; Stoumpos, C. C.; Pedesseau, L.; Katan, C.; Kepenekian, M.; Soe, C. M.; Appavoo, K.; Sfeir, M. Y.; Tretiak, S.; Ajayan, P. M.; Kanatzidis, M. G.; Even, J.; Crochet, J. J.; Mohite, A. D. Extremely efficient internal exciton dissociation through edge states in layered 2D perovskites. *Science* **2017***, 355*, 1288-1292.

12. Raghavan, C. M.; Chen, T.; Li, S.; Chen, W.; Lo, C.; Liao, Y.; Haider, G.; Lin, C.; Chen, C.; Sankar, R. Low-Threshold Lasing from 2D Homologous Organic–Inorganic Hybrid Ruddlesden–Popper Perovskite Single Crystals. *Nano Lett.* **2018***, 18*, 3221-3228.

13. Ishihara, T.; Takahashi, J.; Goto, T. Exciton state in two-dimensional perovskite semiconductor $(C_{10}H_{21}NH_3)_2PbI_4$. *Solid State Commun.* **1989***, 69*, 933-936.

14. Evans, H. A.; Wu, Y.; Seshadri, R.; Cheetham, A. K. Perovskite-related ReO_3-type structures. *Nat. Rev. Mater.* **2020***, 5*, 196-213.

15. Daub, M.; Hillebrecht, H. Synthesis, Single-Crystal Structure and Characterization of $(CH_3NH_3)_2Pb(SCN)_2I_2$. *Angew. Chem. Int. Ed.* **2015***, 54*, 11016-11017.

16. Umeyama, D.; Lin, Y.; Karunadasa, H. I. Red-to-black piezochromism in a compressible Pb–I–SCN layered perovskite. *Chem. Mater.* **2016***, 28*, 3241-3244.

17. Xiao, Z.; Meng, W.; Saparov, B.; Duan, H.; Wang, C.; Feng, C.; Liao, W.; Ke, W.; Zhao, D.; Wang, J. Photovoltaic properties of two-dimensional $(CH_3NH_3)_2Pb(SCN)_2I_2$ perovskite: a combined experimental and density functional theory study. *J. Phys. Chem. Lett.* **2016***, 7*, 1213-1218.

18. Dang, Y.; Liu, G.; Song, J.; Meng, L.; Sun, Y.; Hu, W.; Tao, X. Layered Perovskite $(CH_3NH_3)_2Pb(SCN)_2I_2$ Single Crystals: Phase Transition and Moisture Stability. *ACS Appl. Mater. Interfaces* **2020***, 12*, 37713-37721.

19. Li, C.; Tsai, C.; Liao, M.; Su, Y.; Lin, S.; Chueh, C. Stable, color-tunable 2D SCN-based perovskites: revealing the critical influence of an asymmetric pseudo-halide on constituent ions. *Nanoscale* **2019***, 11*, 2608-2616.

20. Izumi, F.; Momma, K. Three–dimensional visualization in powder diffraction. *Solid State Phenom.* **2007***, 130*, 15-20.

21. Krause, L.; Herbst-Irmer, R.; Sheldrick, G. M.; Stalke, D. Comparison of silver and molybdenum microfocus X-ray sources for single-crystal structure determination. *J. Appl. Crystallogr.* **2015***, 48*, 3-10.

22. Sheldrick, G. M. SHELXT–Integrated space-group and crystal-structure determination. *Acta Crystallogr. , Sect. A* **2015***, 71*, 3-8.

23. Sheldrick, G. M. A short history of SHELX. *Acta Crystallogr. , Sect. A* **2008***, 64*, 112-122.

24. Spek, A. L. Single-crystal structure validation with the program *PLATON*. *J. Appl. Crystallogr.* **2003***, 36*, 7-13.

25. Kresse, G.; Hafner, J. Ab initio molecular dynamics for liquid metals. *Phys. Rev. B* **1993***, 47*, 558-561.

26. Kresse, G.; Hafner, J. Ab initio molecular–dynamics simulation of the liquid-metal–amorphous-semiconductor transition in germanium. *Phys. Rev. B* **1994***, 49*, 14251-14269.

27. Kresse, G.; Furthmüller, J. Efficiency of ab–initio total energy calculations for metals and semiconductors using a plane-wave basis set. *Comput. Mater. Sci.* **1996***, 6*, 15-50.

28. Kresse, G.; Furthmüller, J. Efficient iterative schemes for ab initio total–energy calculations using a plane–wave basis set. *Phys. Rev. B* **1996***, 54*, 11169-11186.

29. Kresse, G.; Joubert, D. From ultrasoft pseudopotentials to the projector augmented–wave method. *Phys. Rev. B* **1999***, 59*, 1758-1775.

30. Krukau, A. V.; Vydrov, O. A.; Izmaylov, A. F.; Scuseria, G. E. Influence of the exchange screening parameter on the performance of screened hybrid functionals. *J. Chem. Phys.* **2006***, 125*, 224106.

31. Yin, W.; Yang, J.; Kang, J.; Yan, Y.; Wei, S. Halide perovskite materials for solar cells: a theoretical review. *J. Mater. Chem. A* **2015***, 3*, 8926-8942.

32. Ganose, A. M.; Jackson, A. J.; Scanlon, D. O. sumo: Command-line tools for plotting and analysis of periodic *ab initio* calculations. *J. Open Source Software* **2018***, 3*, 717.

33. Jaffe, A.; Lin, Y.; Beavers, C. M.; Voss, J.; Mao, W. L.; Karunadasa, H. I. High-pressure single-crystal structures of 3D lead-halide hybrid perovskites and pressure effects on their electronic and optical properties. *ACS Cent. Sci.* **2016***, 2*, 201-209.

34. Kim, G. Y.; Senocrate, A.; Yang, T.; Gregori, G.; Grätzel, M.; Maier, J. Large tunable photoeffect on ion conduction in halide perovskites and implications for photodecomposition. *Nat. Mater.* **2018***, 17*, 445-449.

35. Slotcavage, D. J.; Karunadasa, H. I.; McGehee, M. D. Light-induced phase segregation in halide-perovskite absorbers. *ACS Energy Lett.* **2016***, 1*, 1199-1205.

36. Hutter, E. M.; Muscarella, L. A.; Wittmann, F.; Versluis, J.; McGovern, L.; Bakker, H. J.; Woo, Y.; Jung, Y.; Walsh, A.; Ehrler, B. Thermodynamic stabilization of mixed-halide perovskites against phase segregation. *Cell Rep. Phys. Sci.* **2020***, 1*, 100120.

37. Bailey, R.; Kozak, S.; Michelsen, T.; Mills, W. Infrared spectra of complexes of the thiocyanate and related ions. *Coord. Chem. Rev.* **1971***, 6*, 407-445.

38. Nishida, J.; Breen, J. P.; Lindquist, K. P.; Umeyama, D.; Karunadasa, H. I.; Fayer, M. D. Dynamically Disordered Lattice in a Layered Pb-I-SCN Perovskite Thin Film Probed by Two-Dimensional Infrared Spectroscopy. *J. Am. Chem. Soc.* **2018***, 140*, 9882-9890.

39. Goodwin, A. L.; Calleja, M.; Conterio, M. J.; Dove, M. T.; Evans, J. S.; Keen, D. A.; Peters, L.; Tucker, M. G. Colossal positive and negative thermal expansion in the framework material $Ag_3[Co(CN)_6]$. *Science* **2008***, 319*, 794-797.

40. Serra-Crespo, P.; Dikhtiarenko, A.; Stavitski, E.; Juan-Alcañiz, J.; Kapteijn, F.; Coudert, F.; Gascon, J. Experimental evidence of negative linear compressibility in the MIL-53 metal–organic framework family. *CrystEngComm* **2015***, 17*, 276-280.

41. Cairns, A. B.; Goodwin, A. L. Negative linear compressibility. *Phys. Chem. Chem. Phys.* **2015***, 17*, 20449-20465.

42. Hodgkins, T. L.; Savory, C. N.; Bass, K. K.; Seckman, B. L.; Scanlon, D. O.; Djurovich, P. I.; Thompson, M. E.; Melot, B. C. Anionic order and band gap engineering in vacancy ordered triple perovskites. *Chem. Commun.* **2019***, 55*, 3164-3167.

43. Ganose, A. M.; Savory, C. N.; Scanlon, D. O. $(CH_3NH_3)_2Pb(SCN)_2I_2$: a more stable structural motif for hybrid halide photovoltaics? *J. Phys. Chem. Lett.* **2015***, 6*, 4594-4598.

44. Younts, R.; Duan, H. S.; Gautam, B.; Saparov, B.; Liu, J.; Mongin, C.; Castellano, F. N.; Mitzi, D. B.; Gundogdu, K. Efficient Generation of Long-Lived Triplet Excitons in 2D Hybrid Perovskite. *Adv. Mater.* **2017***, 29*, 1604278.

45. Karim, M. M.; Ganose, A. M.; Pieters, L.; Winnie Leung, W.; Wade, J.; Zhang, L.; Scanlon, D. O.; Palgrave, R. G. Anion distribution, structural distortion, and symmetry-driven optical band gap bowing in mixed halide Cs_2SnX_6 vacancy ordered double perovskites. *Chem. Mater.* **2019***, 31*, 9430-9444.

46. Ganose, A. M.; Savory, C. N.; Scanlon, D. O. Electronic and defect properties of $(CH_3NH_3)_2Pb(SCN)_2I_2$ analogues for photovoltaic applications. *J. Mater. Chem. A* **2017***, 5*, 7845-7853.

47. Bradley, C.; Cracknell, A. *The mathematical theory of symmetry in solids;* Oxford University Press: 1972; .

Mixed-anion hybrid organic-inorganic layered perovskites, $(MA)_2PbI_{2-x}Br_x(SCN)_2$, exist across a broad compositional range ($0 \leq x < 1.6$). The optical band gap increases by Br-substitution in agreement with density functional theory calculations.